



Remote sensing assessment of oil spills near a damaged platform in the Gulf of Mexico

Shaojie Sun^a, Chuanmin Hu^{a,*}, Oscar Garcia-Pineda^b, Vassiliki Kourafalou^c,
Matthieu Le Hénaff^{d,e}, Yannis Androulidakis^c

^a College of Marine Science, University of South Florida, 140 Seventh Avenue South, St. Petersburg, FL 33701, USA

^b Water Mapping LLC, 3010 Coral Strip Parkway, Gulf Breeze, FL 32563, USA

^c Rosenstiel School of Marine and Atmospheric Science, University of Miami, 4600 Rickenbacker Causeway, Miami, FL 33149, USA

^d Cooperative Institute for Marine and Atmospheric Studies, University of Miami, 4600 Rickenbacker Causeway, Miami, FL 33149, USA

^e NOAA Atlantic Oceanographic and Meteorological Laboratory, 4301 Rickenbacker Causeway, Miami, FL 33149, USA

ARTICLE INFO

Keywords:

Oil spill
Optical remote sensing
Taylor Energy
MC-20
Gulf of Mexico
Hurricane

ABSTRACT

An oil platform in the Mississippi Canyon 20 (MC-20) site was damaged by Hurricane Ivan in September 2004. In this study, we use medium- to high-resolution (10–30 m) optical remote sensing imagery to systematically assess oil spills near this site for the period between 2004 and 2016. Image analysis detects no surface oil in 2004, but ~40% of the cloud-free images in 2005 show oil slicks, and this number increases to ~70% in 2006–2011, and > 80% since 2012. For all cloud-free images from 2005 through 2016 (including those without oil slicks), delineated oil slicks show an average oil coverage of 14.9 km²/image, with an estimated oil discharge rate of 48 to ~1700 barrels/day, and a cumulative oil-contaminated area of 1900 km² around the MC-20 site. Additional analysis suggests that the detected oil slick distribution can be largely explained by surface currents, winds, and density fronts.

1. Introduction

During Hurricane Ivan in September 2004, the oil platform and 25 of the 28 connected wells at the Taylor Energy's Mississippi Canyon 20 (MC-20) site, located in the northern Gulf of Mexico (GoM), were damaged and impacted. Subsequently, oil was found leaking, which was reported as the Taylor Energy oil spill or MC-20 oil spill (Herbst et al., 2016; Warren et al., 2014). Although mitigation efforts have taken place (including removal of the platform deck and subsea debris, decommissioning of the oil pipeline, and plugging 9 of the 25 impacted wells), there has been a continuous oil discharge from the platform site. Beginning in September 2014, over 7 months of near-daily aircraft overflights reported oil sheen observations, with an oil slick generally about 1.6 km wide and 9 km long, and an average oil coverage area of 20 km² (BSEE, 2017). The United States Bureau of Safety and Environmental Enforcement (BSEE) estimated that the oil discharge could continue for 100 years or more if left uncontrolled (BSEE, 2017). This crude oil spill from the MC-20 site is also documented in the National Response Center (NRC) reports (NRC, 2018), containing information like spill locations, spill materials, spill size, etc., with involved material documented as crude oil (NRC, 2018; NOAA, 2013). The NRC reports,

however, depend largely on unverified reporting from responsible parties (polluters) and third parties, and therefore its reported slick size information was found to be significantly underestimated (Daneshgar Asl et al., 2016). Moreover, those traditional airborne and shipborne surveys are often too limited spatially and temporally to construct statistics about the discharged oil, as they often result in data gaps. Satellite remote sensing, which serves as a vital tool in response to oil spills (Leifer et al., 2012), provides frequently synoptic observations of the MC-20 oil locations over the entire spill period (since 2004) and may fill these data gaps in objectively assessing the oil spill near the MC-20 site.

The proximity of the MC-20 site to the Mississippi River Delta suggests that the oil slick extensions and fate are under the direct effect of the river plume dynamics, which play a significant role in the circulation around the Delta and over the broader Northern Gulf circulation (Walker et al., 2005; Schiller et al., 2011; Androulidakis and Kourafalou, 2013; Androulidakis et al., 2015). The brackish plume may either extend over the MC-20 site, forming a near-surface vertical barrier layer, or determine the oil transport pathways along the river-induced fronts. Based on satellite (remote sensing imagery) and field (drifters, ship-borne measurements) observations, Androulidakis et al.

* Corresponding author.

E-mail address: huc@usf.edu (C. Hu).

(2018) showed that the locations of the river's multiple fronts (outer and inner density fronts) are vital for the evolution and fate of the material at the sea surface that originates from the MC-20 site. The buoyancy-driven Mississippi plume waters generally reveal three major pathways where the Coriolis effect is important (Garvine and Monk, 1974; Kourafalou et al., 1996): an anticyclonic bulge around the Delta, a “downstream” coastal current toward the northwestern Gulf shelves, and an “upstream” current toward the northeastern shelves (Schiller et al., 2011; Zhang et al., 2012; Androulidakis et al., 2015). Although several other atmospheric (e.g. winds) and oceanic (e.g. local eddies, Loop Current) conditions determined the oil spill fate during the DeepWater Horizon (DWH) accident in 2010 (Walker et al., 2011; Le Hénaff et al., 2012), the river plume contribution was vital to the spreading of the hydrocarbons over the Gulf and especially around the Mississippi River Delta region (Kourafalou and Androulidakis, 2013). The use of remote sensing imagery benefits both the observation of oil slick dynamics over short-term (a few hours to a few consecutive days) and the long-term oil distribution frequency near the Mississippi River Delta region, enabling the study of river plume impacts on oil slick spreading in a region under strong influence of the Mississippi River plume. Despite sporadic field and airborne surveys, no comprehensive long-term picture currently exists regarding the oil spill near the MC-20 site. Therefore, there are two main goals in this study: first to geo-statistically analyze oil slicks using medium- to high-resolution (10–30 m) satellite imagery around the MC-20 site from September 2004 to December 2016; and to study how atmospheric and ocean conditions affect the oil slick distributions observed in remote sensing imagery in this region under strong river plume influence.

2. Data and methods

The MC-20 site is located approximately 17 km offshore from the Mississippi Delta in the GoM (Fig. 1). The location is in the frontal region of the Mississippi river plume, with associated wells at a water depth of 145 m. This MC-20 site is ~60 km away from the DWH (Macondo) blowout location (Fig. 1). The catastrophic explosion and sinking of the DWH oil platform on 20 April 2010 caused the second largest marine oil spill in history (McNutt et al., 2012; Murphy et al., 2016). The Macondo well emitted 3.19 million barrels of crude oil into the northern GoM (McNutt et al., 2012; U.S. v. BP et al., 2015) until the wellhead was finally capped on 15 July 2010.

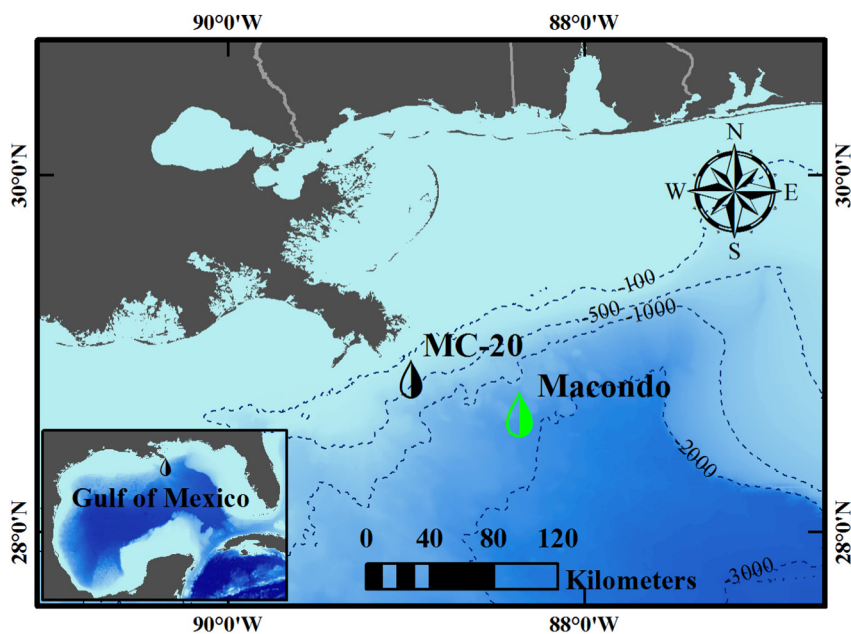


Fig. 1. The MC-20 site (black droplet top: latitude 28.94, longitude -88.97 , which also applies to the following figures) is 17 km offshore of the Mississippi River Delta in the Gulf of Mexico (GoM) at a water depth of 145 m. The 2010 DeepWater Horizon (DWH) oil spill in the Macondo site (green droplet top: latitude 28.74, longitude -88.37) is ~60 km southeast of the MC-20 site with a water depth of ~1500 m. The background color in the GoM denotes the water depth, and major bathymetry contours (in units of meters) have been noted on the map.

In optical remote sensing imagery, the contrast between surface oil and non-oil water comes from two sources. The first is the sun glint effect, which enhances the contrast of the otherwise non-observable oil due to the wave-damping effect (Adamo et al., 2009; Hu et al., 2009; Macdonald et al., 1993; Sun and Hu, 2016). The same mechanism affects the Synthetic Aperture Radar (SAR) detection of oil at the ocean surface (Brekke and Solberg, 2005). Depending on the viewing geometry and wind, the oil-water contrast can be either positive or negative in the optical imagery (Hu et al., 2009; Jackson and Alpers, 2010; Lu et al., 2016). The second is the difference between optical properties of oil and water. Crude oil is characterized by high absorption in blue wavelengths (Byfield, 1998) where the increased thickness of oil correlates to decreased reflectance in blue waves (Lu et al., 2013a; Wettle et al., 2009) until oil is too thick for light penetration (Lu et al., 2013b). When oil is emulsified, the water-in-oil emulsion causes strong scattering in the red, near infrared (NIR), and shortwave infrared (SWIR) wavelengths (Bulgarelli and Djavidnia, 2012; Clark et al., 2010; Svejkovsky et al., 2012). A combination of sun glint and optical properties of the oil-water contrast has been used to efficiently characterize oil spills in a marine environment (Bulgarelli and Djavidnia, 2012; Clark et al., 2010; Hu et al., 2009; Leifer et al., 2012; Lu et al., 2013b; Sun et al., 2015).

In this study, for oil slick delineation we mainly used optical remote sensing imagery from Landsat-5 Thematic Mapper (TM), Landsat-7 Enhanced Thematic Mapper Plus (ETM+), Landsat-8 Operational Land Imager (OLI), and Sentinel-2 MultiSpectral Instrument (MSI). Landsat sensors have a nominal resolution of 30 m while MSI has a nominal resolution of 10 m. Oil slicks from the DWH oil spill between April and July 2010 have been shown to reach the MC-20 region (Hu et al., 2011; MacDonald et al., 2015). To avoid confusion from the DWH oil spill, images collected in 2010 around the MC-20 site were not included in this study. Landsat imagery has a revisit time of 16 days alone (Table 1), and 8 days combined (TM with ETM+ in 2004–2011, and ETM+ with OLI in 2013–2016). A total of 513 medium- to high-resolution images (10–30 m) were explored, with 294 cloud-free images found in this region. A summary of the medium- to high-resolution optical imagery used in this study is shown in Tables 1 and 2. The average cloud-free images per year are 26 (excluding year 2004 since the oil spill started in September of that year), 15 of which were taken during favorable sun glint season in the GoM (April–September, from Hu et al., 2009; Sun and Hu, 2016). Thin oil sheens may not be efficiently detected under

Table 1
Characteristics of optical satellite sensors used for the oil spill assessment in the study.

| Sensor | Data available (year) | Spatial resolution (m) | Spectral bands VIS-SWIR | Revisit time (days) |
|----------------|-----------------------|------------------------|----------------------------|---------------------|
| Landsat-5/TM | 2004–2011 | 30 | 6 | 16 |
| Landsat-7/ETM+ | 2004–2016 | 30 (Pan-15) | 7 | 16 |
| Landsat-8/OLI | 2013–2016 | 30 (Pan-15) | 9 | 16 |
| Sentinel-2/MSI | 2015–2016 | 10, 20, 60 | 13 | 10 |

weak glint conditions (Sun and Hu, 2016). Thick/emulsified oil may still be detected because of their different optical properties with respect to seawater (Wettle et al., 2009; Clark et al., 2010). These sampling frequencies (15 and 26 per year for sun glint images and cloud-free images) are comparable to and higher than the global average frequency of chlorophyll at a typical 1-km pixel from the Moderate Resolution Imaging Spectroradiometer (MODIS, every 20 days or 5%, see Feng and Hu, 2016). Therefore, we believe that the sampling frequency of oil slicks by those medium- to high-resolution imagery is statistical meaningful for assessing the oil spills near the MC-20 site.

MODIS imagery, although providing more frequent coverage (i.e., daily images), has a spatial resolution of 250 to 1000 m, which is too coarse to assess this moderate oil spill, for which the typical slick size ranges from 0 (100 m) to a few tens of kilometers. A statistical analysis during the DWH oil spill demonstrated that on average > 50% of 300-m pixels contain thick oil of < 6.6% of a 300-m pixel (Sun et al., 2016). For 1-km pixels, the sub-pixel percent cover is much lower than 1.0%. Thus, assessing the oil spill near the MC-20 region using MODIS imagery may fail to detect small slicks in oil presence/absence frequency analysis and add uncertainties in statistical analysis of oil slick area. However, occasionally large slicks (tens of kilometers in length and a few kilometers wide) under sun glint conditions can still be detected in MODIS imagery. Therefore, MODIS imagery was used in this study to detect the presence of oil slicks during the initial leaking stage of the spill when Landsat imagery failed to detect slicks in September–December 2004. Moreover, MODIS imagery was used in the analysis of short-term oil slick dynamics to enable more observations of the oil slicks in a few consecutive days. In addition, MODIS and Visible Infrared Imaging Radiometer Suite (VIIRS, 375 to 750 m in spatial resolution) chlorophyll concentration maps were also used to identify the river plume spreading in tandem with the detected oil slicks.

Finally, same day SAR imagery was used to cross-check with results from optical imagery analysis. SAR/optical imagery groups within two days were used with a numerical model and ocean color data to understand short-term dynamics of oil slicks near the MC-20 site.

TM, ETM+, OLI, and MSI Level-1 data were obtained from USGS/EarthExplorer, and then processed to Rayleigh-corrected Reflectance ($R_{rc}(\lambda)$, dimensionless) using the ACOLITE software (version V20161207.0). Red-Green-Blue composites were generated for visual inspection for all four sensors: OLI (R: 655, G: 561, B: 483 nm), ETM+ (R: 661, G: 561, B: 479 nm), TM (R: 660, G: 571, B: 486 nm) and MSI (R: 664, G: 560, B: 497 nm). Sun glint strength of the Landsat imagery was evaluated using sun glint coefficient (L_{GN} , in units of sr^{-1}), estimated with the Cox and Munk (1954) model, wind speed, and solar and satellite geometry. Wind speed was retrieved from the Reanalysis-2 wind speed product of the National Centers for Environmental Prediction

(NCEP). Solar and satellite geometry of Landsat was calculated using the “Landsat Angles Creation Tools” from USGS (<https://landsat.usgs.gov/solar-illumination-and-sensor-viewing-angle-coefficient-file>).

MODIS (on both Terra and Aqua) Level-0 data from September to December 2004 and 7–9 May 2015 were obtained from NASA Goddard Space Flight Center (GSFC) and processed to $R_{rc}(\lambda)$ using the SeaWiFS Data Analysis System (SeaDAS, version 7.3), and then resampled to 250 m spatial resolution using a sharpening scheme and mapped to an equidistant cylindrical projection. RGB composites were generated using the R_{rc} bands (R: 645, G: 555, B: 459 nm). Chlorophyll-a concentration Level-2 data from MODIS Aqua and VIIRS in 5–10 May 2015 were obtained from NASA/GSFC, and mapped to an equidistant cylindrical projection at 1 km spatial resolution.

SAR images used in this study were processed and analyzed as follows: First, a preliminary inspection of the SAR imagery was used to determine the overall ocean features. The texture of the image was evaluated to determine the wind conditions (Garcia-Pineda et al., 2008). When regions of very low wind speeds are present, ripple-free water and biogenic films create irregular, radar-dark regions that are difficult to distinguish from actual oil slicks. The SAR images used for this study were acquired under optimal wind conditions and the oil slick detected from the MC-20 site was clearly distinguishable. After initial inspection, a Textural Classifier Neural Network Algorithm (TCNNA) was applied to identify floating oil layers in a semi-supervised operation (Garcia-Pineda et al., 2008). The TCNNA is conditioned on a training set of SAR features of interest (i.e., floating oil) that previously have been identified by an operator over the natural hydrocarbon seep locations in the GoM (Garcia-Pineda et al., 2008, 2009). The final output of the TCNNA algorithm is a polygon that delineates the area of the slick. More details of the SAR processing can be found in Garcia-Pineda et al. (2008, 2009, 2010).

As mentioned above, oil slicks show spatial contrast from nearby water in optical remote sensing imagery because 1) oil has different optical properties from water and 2) oil can change the surface roughness, thus leading to redistribution of reflected light under sun glint conditions. In this study, oil slicks were identified as follows: 1) color stretched RGB images were visually inspected to detect spatial anomalies; 2) R_{rc} spectra from the anomalies were then diagnosed to rule out oil look-alikes (Hu et al., 2015). More details on the oil identification can be found in Sun et al. (2015). Then, for statistical analysis, the identified oil slicks were all counted for presence/absence in order to estimate oil appearance frequency. In this analysis, only slicks that follow the following rules were delineated and used in the areal statistical analysis: 1) slicks that originated from the MC-20 site and not blocked by clouds, which were treated as major slicks here; 2) smaller slicks near the major slicks. For example, in most cases, the major oil slicks originated from the MC-20 site and extended to one direction of the site (Fig. 2). In Fig. 2d, although the slicks indicated by the arrows can be inferred to be parts of major slicks originated from the MC-20 site, those slicks were only counted for the analysis of presence/absence frequency statistics; they were not delineated because an incomplete slick would not fit the purpose of areal statistical analysis. As a result, major slicks under cloud-free conditions (Fig. 2a and b), partially blocked by small clouds (Fig. 2c), and small slicks detached from major slick (Fig. 2b), were delineated manually using ArcMAP (version 10.3) software. ETM+ imagery suffers from scan line correction failure since 2003 (<https://landsat.usgs.gov/landsat-7>), causing line gaps (evenly

Table 2

Number of cloud-free (CF) images each year and the number of CF images in sun glint favorable period (April–September) in each year.

| Year | 2004 | 2005 | 2006 | 2007 | 2008 | 2009 | 2011 | 2012 | 2013 | 2014 | 2015 | 2016 |
|-------------------------|------|------|------|------|------|------|------|------|------|------|------|------|
| # CF images | 8 | 27 | 26 | 25 | 24 | 28 | 26 | 14 | 22 | 24 | 25 | 45 |
| # CF images APR-SEPT | 2 | 12 | 15 | 17 | 12 | 16 | 14 | 10 | 14 | 16 | 14 | 26 |

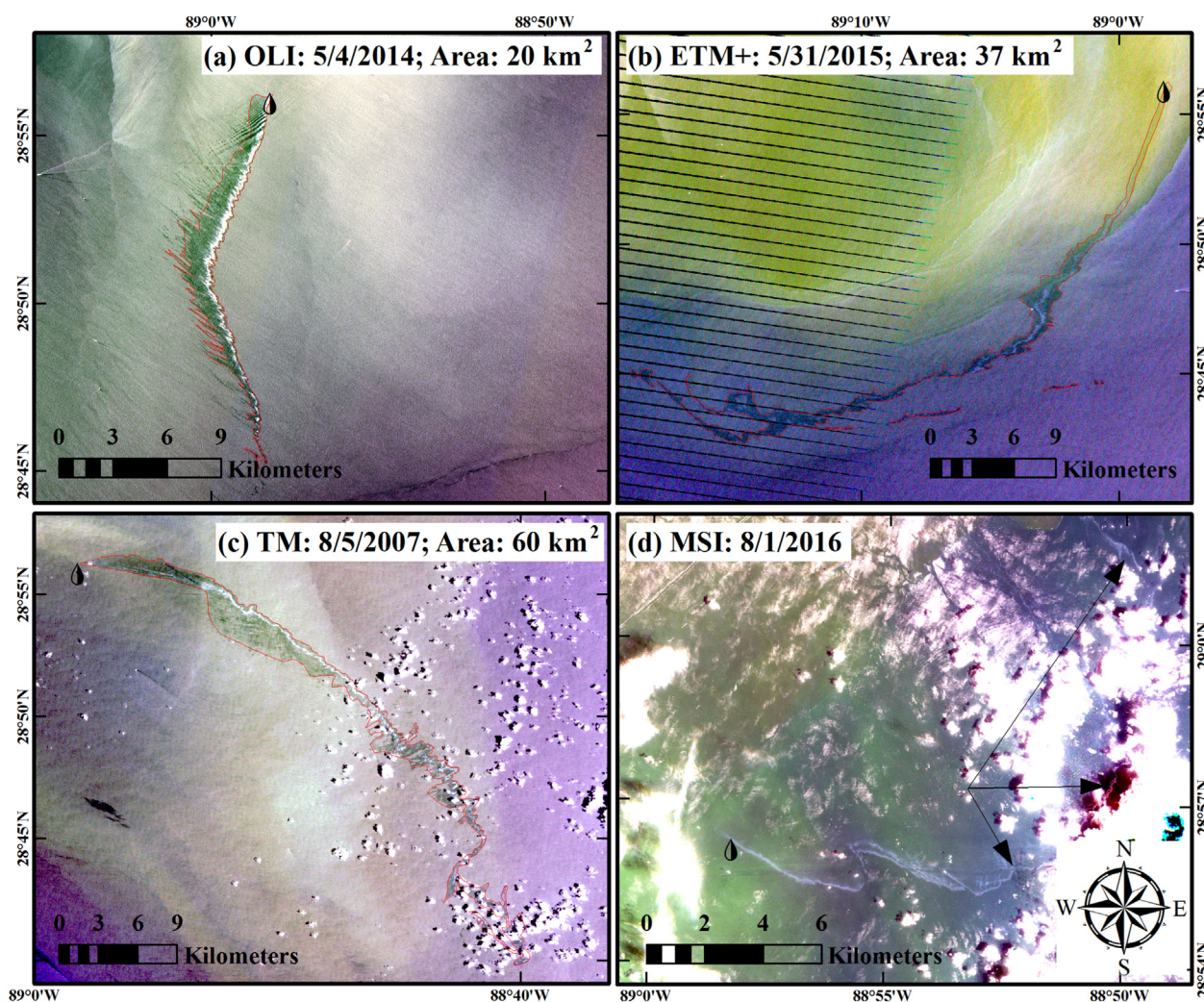


Fig. 2. Oil slicks captured by different sensors: a) OLI; b) ETM+; c) TM; d) MSI. They all appear to have originated from the MC-20 site, with different orientations. Delineated oil slick areas are annotated in (a)–(c). Oil slicks partially blocked by clouds, as shown in the example in (d), were not used for area estimates in this study.

distributed black lines in the left part of Fig. 2b) in all ETM+ scenes since then. Fortunately, the MC-20 location is in the center of the image (Fig. 2b), where the image is least affected by this scan line correction off issue. When oil slicks extend long enough to reach these line gap regions, delineated oil slick polygons on both sides of the missing data line were manually re-connected if oil slicks were present on both sides, as shown in Fig. 2b. The swaths of Landsat imagery and Sentinel-2 MSI imagery are large enough to cover the slicks near the MC-20 site. Because only oil slicks originated from the MC-20 site were considered, the impact of natural oil seeps was minimized in this study.

Simulated fields of surface currents were used to describe the ocean circulation over the study region and compare it with the oil spreading detected by the satellites. The simulation was based on the Hybrid Coordinate Ocean Model (HYCOM; <https://hycom.org/>), implemented at a 1/50° (~1.8 km) resolution and 32 vertical levels over the GoM (GoM-HYCOM 1/50; Le Hénaff and Kourafalou, 2016). Based on a combination of various vertical coordinates (hybrid model), the HYCOM model is particularly suitable for regional domains with complex topography of wide shelves, steep slopes, and deep oceanic areas such as the GoM (Bleck, 2002; Chassignet et al., 2006; Kourafalou et al., 2009; Halliwell et al., 2009). The GoM-HYCOM 1/50 simulation employed here was forced at the surface by the NAVy Global Environmental Model (NAVGEM, 1/2° resolution at 3 hourly frequency), and benefited from realistic river representation. The simulated fields used in this study are part of a long-term simulation that assimilates

observations (based on an Ensemble Optimal Interpolation scheme) and provides publicly available daily forecast ocean fields of the GoM in a weekly basis operated by the Coastal and Shelf Modeling Group (University of Miami/RSMAS; <http://coastalmodeling.rsmas.miami.edu/>). GoM-HYCOM 1/50 uses daily river forcing for the 15 larger rivers in the U.S. part of the domain, including around the Mississippi Delta, while other rivers are represented with their monthly climatology. The river discharge data were obtained through the U.S. Geological Survey (<https://www.usgs.gov/>) and the Army Corps of Engineers. The high-resolution (~1.8 km) of the model in combination with the use of the updated river parameterization by Schiller and Kourafalou (2010), is adequate to efficiently resolve mesoscale and coastal processes around the Mississippi Delta (Le Hénaff and Kourafalou, 2016), where the oil source is located. The river plume dynamics and the formation of the accompanying strong density fronts, dominant over the region around the Mississippi, have been found relevant to the evolution of the shape and orientation of the oil patches during both short-term (a few hours after their formation) and long-term (pathways over a few days and fate) periods (Kourafalou and Androulidakis, 2013; Androulidakis et al., 2018).

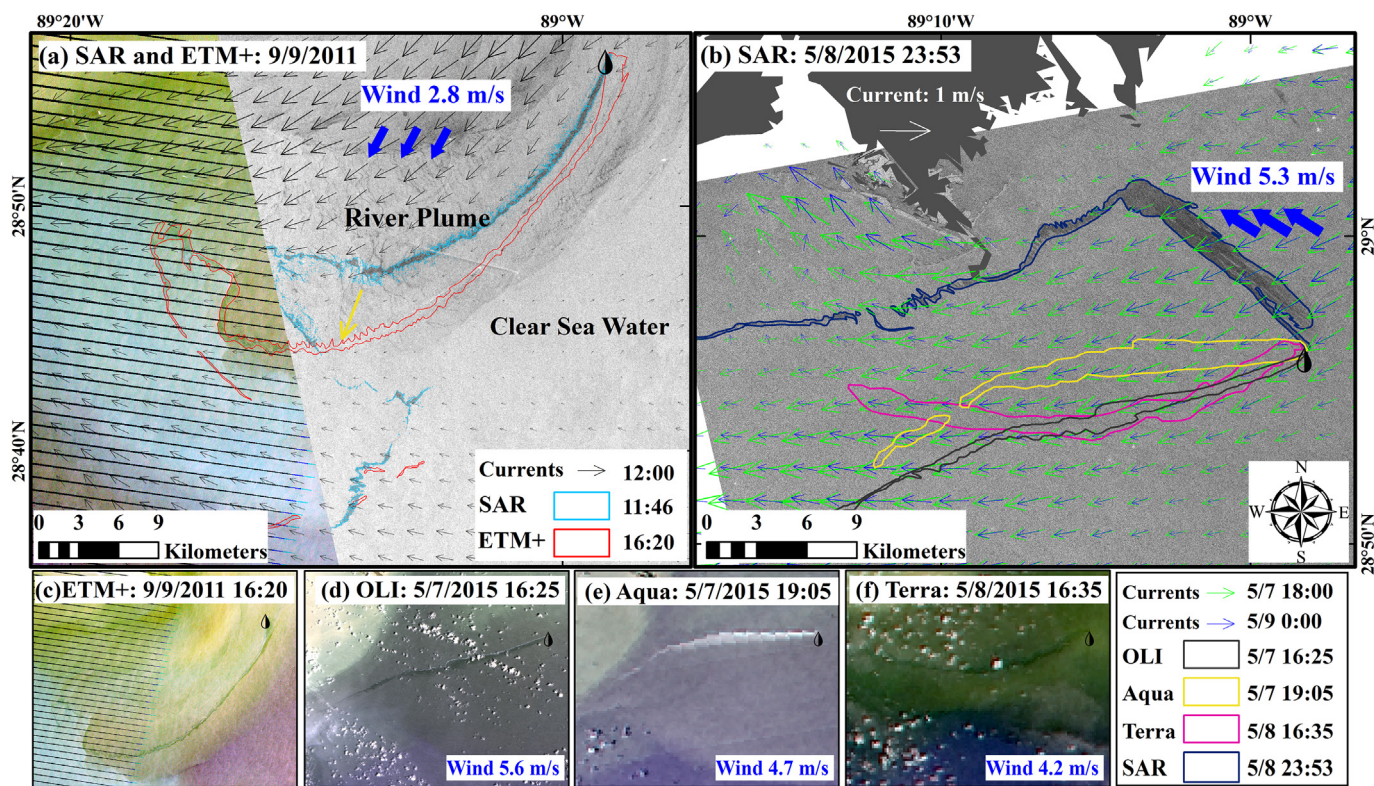


Fig. 3. a) Same day SAR (COSMO-SkyMed-4 collected on 9/9/2011, UTC 11:46, with spatial resolution of 30 m; Dark grey area indicates the River Plume and light grey area the clear sea water; Part of the slick tale was missing in the SAR image because of the image footprint limit) and ETM+ (9/9/2011, UTC 16:20, left part of the image and the entire slick captured by ETM+ was displayed in(c) with delineated oil slick). Four images of oil slicks captured by optical and SAR imagery in two consecutive days: b) SAR acquired by RADARSAT-2 (spatial resolution: 6 m) on 5/8/2015 UTC 23:53, with colored slicks representing those delineated from images in (d)–(f) (legend shown in the bottom right corner); d) OLI on 5/7/2015 UTC 16:25; e) MODIS/Aqua on 5/7/2015 UTC 19:05; and f) MODIS/Terra on 5/8/2015 UTC 16:35. The arrows in (a) and (b) indicate simulated surface current fields, where the current velocity scale in (b) applies to both (a) and (b). The thick blue arrows represent the mean wind direction, estimated between both images on panel a and between the last two images (16:35–23:53, 5/8/2015) in panel b. Wind direction does not change much between 5/7/2015 and 5/8/2015, with a standard deviation of 12.6° over the two days.

3. Results

3.1. Short-term dynamics

Taking advantage of occasions when distinct remote sensing observations of the oil slicks are available a few hours apart or over a few consecutive days, here we analyze the short-term dynamics of oil slicks, together with the wind conditions and the simulated current fields over the MC-20 region. Fig. 3a shows two images of the same slick, captured ~4.5 h apart by SAR and ETM+ on September 9, 2011. The slick on both images generally followed the modeled current directions. On Fig. 3a, the darker area represents the river plume area, while the lightest grey area is characterized by clear ocean waters; the simulated currents inside the plume follow the direction of the downstream river current (southwestward), while the currents over the open ocean were northwestward. The oil pathway in both satellite images is aligned with the river front, in agreement with observational findings by Androulidakis et al. (2018). The southern part of the slick (indicated by the yellow arrow in Fig. 3a) was observed to move ~5 km to the southwest during this time period. The modeled average current field (~0.1–0.3 m/s in a southwestward direction, Fig. 3a) alone cannot fully explain the movement. The wind, which had almost the same direction as the current, must have also contributed to the southwestward movement of the slick. With wind and current in different directions, the group of images during 7–8 May 2015 in Fig. 3b displayed the dominance of current and wind on slick movement at different periods. The oil slick was first captured by OLI to the southwest (7 May 2017 16:25; Fig. 3d). Over time it wandered north and south, as observed by

MODIS Aqua (7 May 2017 19:05; Fig. 3e), and Terra (8 May 2017 16:35; Fig. 3f), before heading northwest (8 May 2017 23:53; Fig. 3b blue highlighted). The modeled currents were mostly westward in May 7, with current direction agreeing well with the westward slicks. Current directions near the MC-20 site shows little change between May 7 and May 9, while the simulated currents field does indicate drastic decrease of magnitude in the site region (0.89 m/s at 18:00 May 7 to 0.39 m/s at 0:00 May 9). Both wind speed and direction showed little changes over the two days. However, the wind direction agreed well with the northward slick observed at 23:53 on May 8 (Fig. 3b), indicating apparent wind shift affecting the slick. Obviously, there is a shift, from surface currents to winds, of the driver of the displacement of the oil slicks between May 7 and May 9.

This shift of dominant forces is further revealed in sequential chlorophyll-a concentration from VIIRS and MODIS between 7–10 May 2015 (Fig. 4), which indicates an onshore shift of the river plume. On May 7 and 8, the river plume encompassed the MC-20 site (Fig. 4a and b). On May 9, the MC-20 site was on the outer edge south of the major plume region (Fig. 4c). This plume shift was further confirmed by the chlorophyll-a image on May 10 (Fig. 4d). The northward shift of the river front allowed the onshore propagation of the oil toward the Delta, visible on May 9 (Fig. 4c), in contrast to the previous days, when the front was over the oil source, leading the oil directly westward. However, even when shifted northward, the oil eventually reached a strong river-induced front and was directed westward along the downstream current in agreement with the observational study at the MC-20 site by Androulidakis et al. (2018). The evolution of the river plume determined the hydrocarbon pathways and can keep the oil away from the

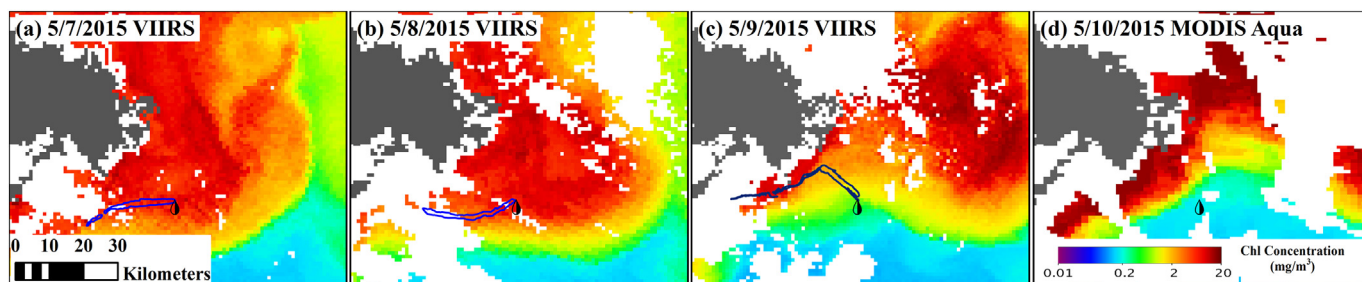


Fig. 4. Chlorophyll-a concentration in the Mississippi River Delta indicates river plume between 5/7/2015 and 5/10/2015. Oil slicks detected on 19:05 5/7/2015, 16:35 5/8/2015 and 23:53 5/8/2015 are added to (a), (b) and (c), respectively.

Delta, especially in cases where the outer river front is located north of the MC-20 site (Androulidakis et al., 2018); similar interactions were discussed for hydrocarbons released at the Macondo well during the DWH incident (Kourafalou and Androulidakis, 2013). Downwelling-favorable (i.e., southeasterly) winds may determine the location of the river front and then push the surface oil toward the front, where it can be trapped and then follow the prevailing upstream (northeastward) or downstream (westward) river current, as demonstrated in Fig. 4c.

3.2. Statistical analysis from 2004 to 2016

Observations from ETM+ in September–December 2004 (Fig. 5a) did not reveal any oil slicks, while < 50% of the cloud-free images in 2015 showed slicks. This percentage increased through 2007 (79%) and fluctuated from 2008 to 2011 (ranging from 57% to 93%). Since 2012, however, the percentage was relatively stable between 71 and 100%. Similar results were found from TM, OLI and MSI observations in the

same period: 0% in 2004, < 50% in 2005, 89% in 2006 and relatively stable since 2012 (> 90%) (Fig. 5b). Differences between ETM+ and other sensors also exist: 53% of the cloud-free ETM+ images in 2006 showed oil slicks while this percentage was as 89% for TM images in the same year; in 2008, 2009, 2011, the ratio of oil-presence to cloud-free images was 75%, 93% and 57% for ETM+, respectively, and was 67%, 64% and 83% for TM, respectively. Combining all sensors together, the ratio of oil-presence images to cloud-free images was 0% in 2004, ~40% in 2005, ~70% in 2006–2011 and > 80% since 2012 (most of the years showed > 90%, Table 3). Fig. 5c shows delineated slick areas from individual images from all sensors. For oil-presence images, the slick area ranged from 0.06 to 394 km², with an average oil coverage area of 19.0 km² and a median area of 7.6 km² after excluding those extremely large oil slicks (> mean + 2 * standard-deviation). For all cloud-free images combined, the average oil coverage area was estimated to be 14.9 km²/image between 2005 and 2016 (with 2010 excluded). From the size of delineated oil slicks, no clear trend has been

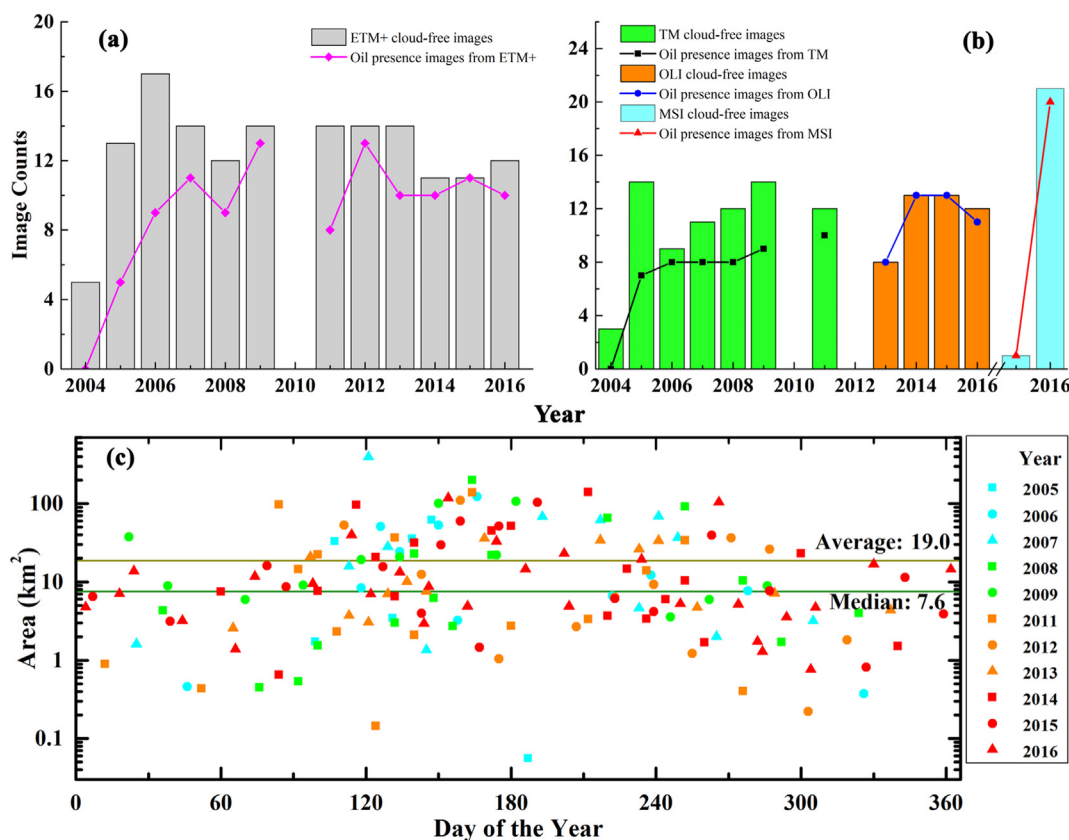


Fig. 5. Number of cloud-free images (vertical bars) and number of oil-presence images (lines) around the MC-20 site between 2004 and 2016 captured by a) ETM+ and b) TM, OLI, and MSI. c) Oil slick area from individual images of all sensors; The average and median area of slicks presented in the graph are for oil-presence images only, after excluding those extremely large oil slicks (> mean + 2 * standard-deviation).

Table 3

Percentage ratio of oil presence images to all cloud-free images (including those without sun glint) combining observations from all four sensors.

| Year | 2004 | 2005 | 2006 | 2007 | 2008 | 2009 | 2010 | 2011 | 2012 | 2013 | 2014 | 2015 | 2016 |
|------|------|------|------|------|------|------|------|------|------|------|------|------|------|
| % | 0 | 44 | 65 | 76 | 71 | 79 | – | 69 | 93 | 82 | 96 | 100 | 91 |

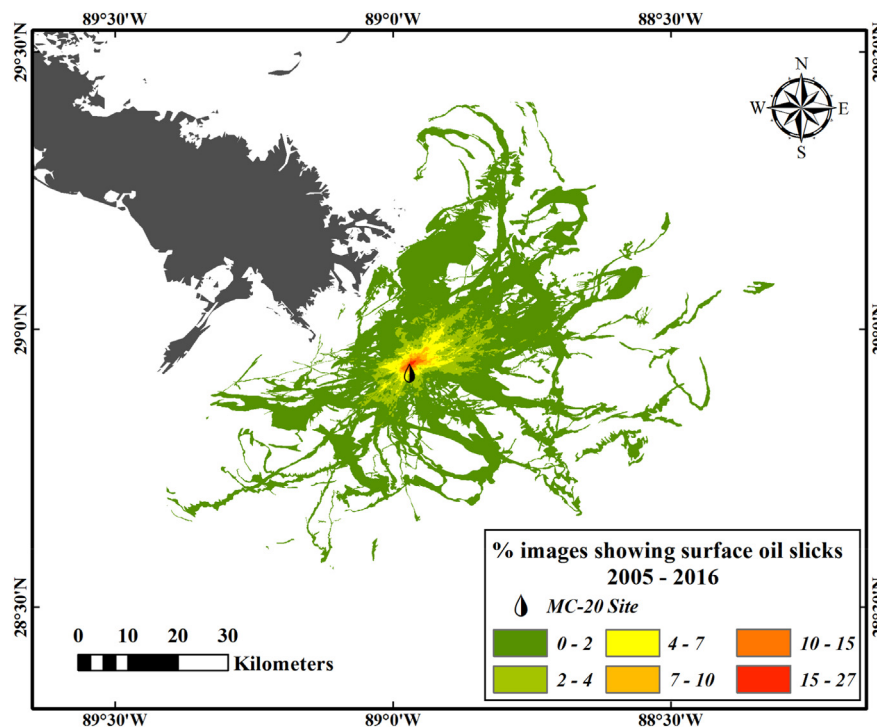


Fig. 6. Oil appearance frequency from all cloud-free images (including those without sun glint) in 2005–2016, which shows a cumulative area of 1888 km² near the MC-20 site. The appearance frequency ranges from 0.5% to 27% in this cumulative footprint map.

observed from 2005 to 2016. However, there is an obvious seasonal cycle: most of the large slicks (> 19 km²) were detected between April and September each year (Fig. 5c).

From all delineated oil slicks from 2005 through 2016, the cumulative oil footprint shown in Fig. 6 indicates that an area of ~1900 km² over the regions surrounding the Mississippi Delta has been contaminated by oil originated near the MC-20 site. Statistical results shows that 98% of the above polluted areas had oil pollution only occasionally (< 5% of cloud-free observations) while the more frequently oil polluted regions (> 20% of the cloud free observations) had an area of 0.17 km² surrounding the MC-20 site. Although the average oil slick size is 14.9 km²/image, because slicks are mostly narrow, elongated lines around the MC-20 site, only 0.17 km² around the site was covered by oil > 20% of the time. Indeed, this oil appearance frequency map (Fig. 6) is composed largely (> 50%) by oil slick size < 10 km² per image (Fig. 7a), while occasionally (8.6%) by oil slick size > 90 km² per image (Fig. 7a). This slick size frequency explains the more frequent coverage near the MC-20 site but lower frequent coverage away from the site.

The region with high-frequency oil presence (yellow to red in Fig. 6) displays a northeast-southwest pattern around the MC-20 site, which agrees well with the circulation patterns of the Mississippi River plume: an anticyclonic bulge around the Delta (where most oil has concentrated), with influence from the downstream westward current, and/or the northeastward upstream current (Schiller et al., 2011; Zhang et al., 2012; Androulidakis et al., 2015, 2018). The prevailing wind corresponding to all oil-presence images in Fig. 6, however, is to the west and northwest (Fig. 7b). This dominantly northeast-southwest oil coverage pattern suggests that the most frequent slick spreading

orientation is more likely dominated by the river plume induced currents (e.g. Fig. 3a, c–f) rather than directed by the winds. However, slicks derived from sequential images between May 7 and 8 in Fig. 3b indicate that wind can play a major role in the slick spreading near the MC-20 site when river front is located north of the MC-20 and the current is weak. Overall, the distribution of observed northeastward and westward oil slicks agrees well with the downstream westward current and northeastward upstream current of the Mississippi River plume, and the southeast extensions of the oil slicks are likely to be dominated by wind forces (Le Hénaff et al., 2012) or the offshore river plume extensions into the GoM which often occur due to regional ocean dynamics effects, such as the Loop Current and its frontal eddies (Liu et al., 2013; Androulidakis et al., 2018).

3.3. Imagery cross check

Landsat sensors' (TM with ETM+, ETM+ with OLI) image sensing time is offset in 8 days, thus there are no concurrent (i.e., same-day) measurements of the same location from these Landsat sensors. MSI, however, may sometimes sense the same location with OLI/ETM+ in the same day. For example, Fig. 8a and b show oil slicks captured on the same day by OLI and MSI, with a time difference of 15 min. The derived shape, location, distribution and area of oil slicks (38.7 km² vs 39.1 km²) agree well between each other. Fig. 8c and d show the same day ETM+ and SAR imagery over the same location with a time difference of 7.4 h. The detected oil slicks by both sensors, although both extending to the west, display large differences in location, slick shape and distribution. The derived slick areas are 5.6 km² from SAR while 8.1 km² from ETM+. Table 4 summarizes all the same-day image pairs

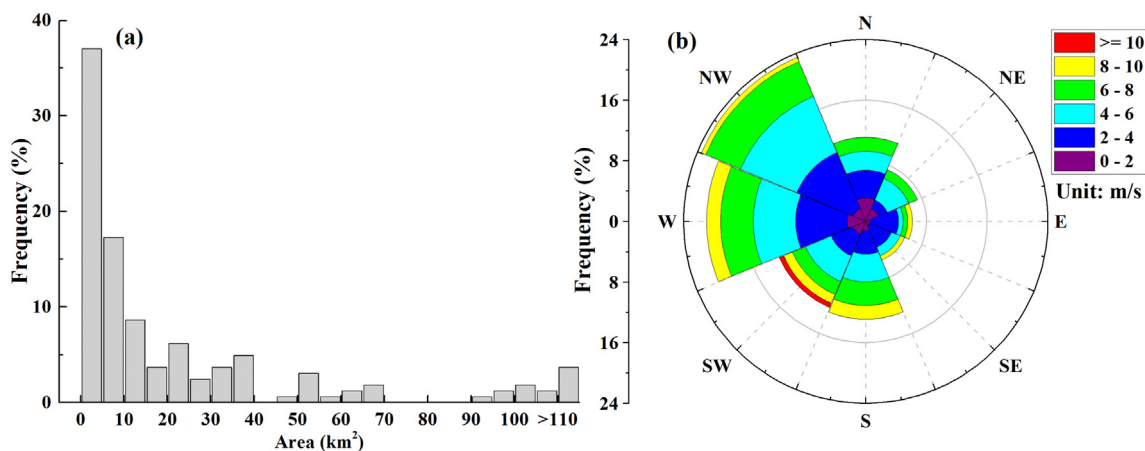


Fig. 7. (a) Area frequency of all delineated oil slicks per image, which include all slicks here contributing to the cumulative oil footprint map in 2005–2016 shown in Fig. 6. (b) Statistics of wind speeds and directions near the MC-20 site at the time of the same delineated slicks. Here the angular axis refers to the direction to which the wind is blowing, and the radial axis refers to the wind speed frequency of particular wind speed range. From the wind rose plot, dominant wind directions are to the west and northwest, and wind speeds are mostly 2–8 m/s for the delineated slicks.

that captured oil slicks over the MC-20 locations with time difference of 8 h or less. The SAR/ETM+ image pair on 9 Sept. 2011 have slick shape and orientation close to each other, though wider slick close to the MC-20 site has been observed in the ETM+ image after 4.5 h (Fig. 3a), which is reflected in the slick area change (8.6 km² in SAR vs 16.5 km² in ETM+) from the MC-20 site to the yellow arrow location in Fig. 3a.

There are also slicks for which the area drastically changed after 4.6 h, like the SAR/OLI image pair on 18 Jan. 2016. As described in Section 3.1, the short term dynamics of oil slicks can be affected by both wind and current conditions, and are strongly influenced by the Mississippi River plume dynamics. Here we use an Unbiased Mean Relative Error (UMRE) to estimate the relative error the delineated slick area in

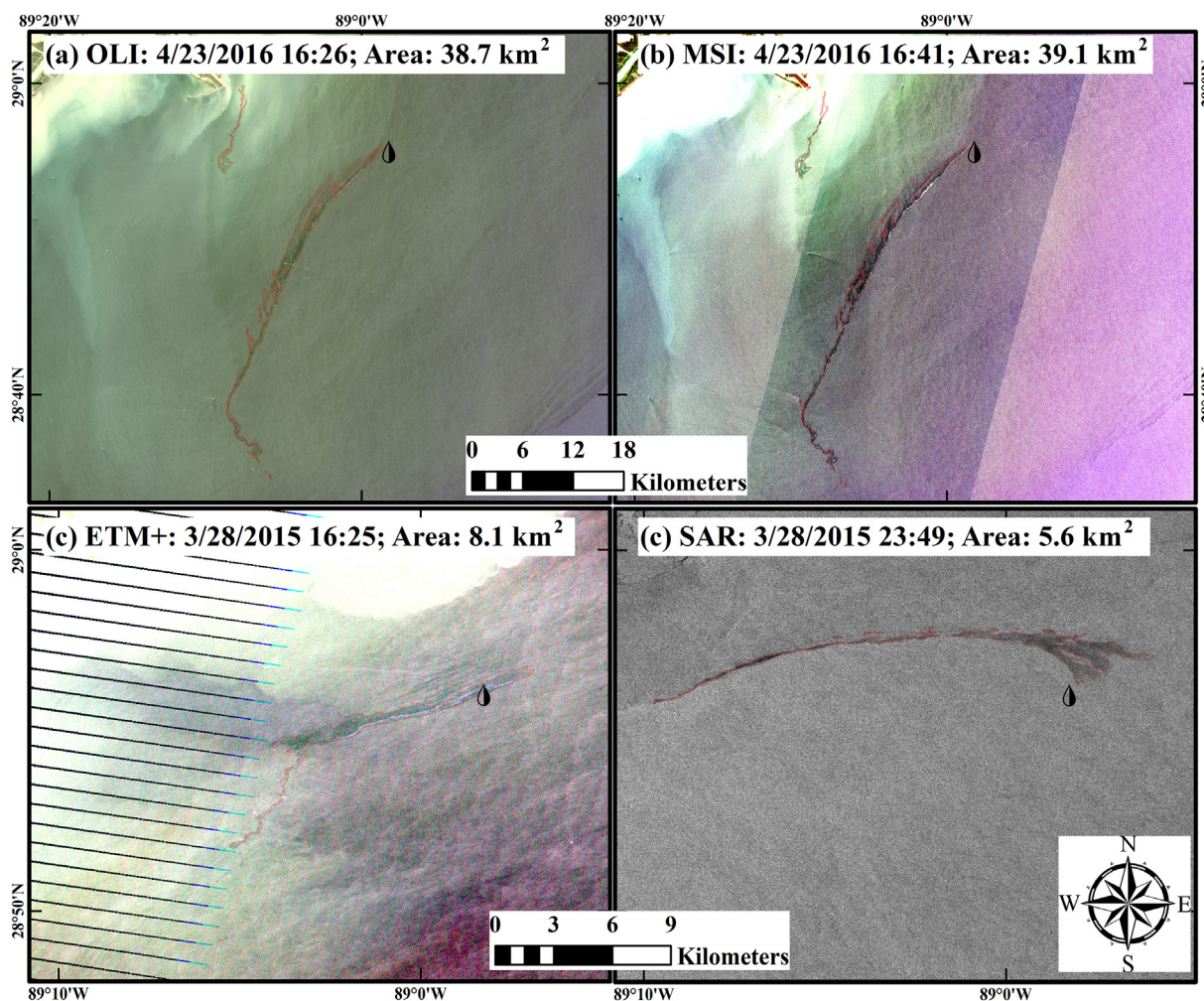


Fig. 8. Examples of oil slick size estimation using same-day image pairs captured by (a) OLI with (b) MSI, and (c) ETM+ with (d) SAR from Radarsat-2.

Table 4

Same-day image pairs between optical sensors and optical/SAR sensors over the MC-20 area. SAR1 is from COSMO-SkyMed-4 with spatial resolution of 30 m, SAR2 from Radarsat-2 with spatial resolution of 6 m, and SAR3 from Sentinel-1A with spatial resolution of 10 m. Note that in the 9/9/2011 image pair, area of the slick part from the MC-20 site to the yellow arrow location in Fig. 3a that captured by both the SAR and ETM+ images was compared in the table.

| Sensor 1 | Date | Time | Area (km ²) | Sensor 2 | Date | Time | Area (km ²) |
|----------|------------|-------|-------------------------|----------|------------|-------|-------------------------|
| SAR1 | 9/9/2011 | 11:46 | 8.6 | ETM+ | 9/9/2011 | 16:20 | 16.5 |
| SAR2 | 3/28/2015 | 23:49 | 5.6 | ETM+ | 3/28/2015 | 16:25 | 8.1 |
| MSI | 12/25/2015 | 16:41 | 3.7 | ETM+ | 12/25/2015 | 16:27 | 2.2 |
| SAR3 | 1/18/2016 | 11:49 | 1.2 | OLI | 1/18/2016 | 16:26 | 6.9 |
| MSI | 4/23/2016 | 16:41 | 39.1 | OLI | 4/23/2016 | 16:26 | 38.7 |
| MSI | 9/30/2016 | 16:46 | 4.9 | OLI | 9/30/2016 | 16:26 | 6.0 |

Table 4, as either of the areas from the two datasets may contain uncertainties:

$$UMRE = \frac{1}{n} \sum_{i=1}^n \left| \frac{x_i - y_i}{0.5x_i + 0.5y_i} \right| \quad (1)$$

where x_i , y_i are the areas of the delineated oil slicks from the two images of the image pair, respectively. The calculated area UMRE is 52.3%, which represents the relative difference of oil slick area caused by oil interpretation uncertainties (i.e., interpretation difference between different sensors) and slick short-term dynamics by the current/wind (as shown in Section 3.1). Because the imaging time as well as observation geometry vary largely among different sensors, these results from the same-day image pairs represent the best estimates of the relative error in oil slick area.

4. Discussions

4.1. Uncertainties

The accuracy of slick size detection through optical imagery relies on sun glint strength. The MSI/OLI pairs on 23 Apr. 2016 and 30 Sept. 2016 agree well in slick distribution and slick areas because all images contain strong sun glint. On the other hand, the slick area detected by ETM+ on 25 Dec. 2015 is significantly lower than the slick area detected by MSI on the same day, partly because of the very low sun glint strength of the two images ($< 10^{-5} \text{ sr}^{-1}$) and partly because of the lower signal-to-noise ratio of ETM+ compared to MSI. Those oil features not captured by the ETM+ image are thin oil, which displays little contrast under very weak sun glint conditions. Therefore, only when sun glint is strong enough can the detection be regarded as accurate. The sun glint strength (L_{GN}) of all cloud-free optical images was estimated and partitioned into two groups for images with and without oil detected. The median value of L_{GN} for the first group ($1.6 \times 10^{-3} \text{ sr}^{-1}$) was found to be about two orders of magnitude higher than for the second group ($2.2 \times 10^{-5} \text{ sr}^{-1}$). The images of the first group were mainly from April to September where sun glint strength is higher than in October through March, when most images of the second group were collected. Similarly, images collected between April and September contributed to only 15% of the oil-absence images, but they contributed to 70% of the oil-presence images. Such a seasonality can also be visualized clearly in the slick area plot in Fig. 5c, with average delineated slick area per image to be 23.8 km² from April to September (from 107 oil presence images), but 8.4 km² from October to March (from 49 oil presence images). Since there is no reason, to our knowledge, why the

oil discharge should change seasonally, we can only assume this is most likely due to the seasonality of sun glint strength. For this reason, the oil presence and footprint estimates are likely biased low.

It is interesting to see that none of the 2004 images between September and December showed oil slicks, possibly due to the same reason as above: most images collected during this period did not show significant sun glint. Indeed, a cloud-free MODIS/Terra image on 28 September 2004 did show oil slicks around the MC-20 site because MODIS could provide much more frequent observations than those medium- to high-resolution sensors. Nevertheless, the many available medium- to high-resolution images from multiple sensors since 2005 should lead to statistically meaningful results even though there may exist systematic biases due to seasonality in oil slick detection, which suggests that the inter-annual changes and long-term trend should be realistic.

4.2. Oil discharge volume

Airborne measurements and cruise surveys reported crude oil featured slicks near the MC-20 site, ranging from oil sheens to oil emulsions as thick as 1–2 mm (BSEE, 2017; Garcia-Pineda, 2016; Herbst et al., 2016; Jones and Holt, 2018). In optical remote sensing imagery, oil emulsions show elevated reflectance in the NIR-SWIR wavelengths (Clark et al., 2010; Sun et al., 2018). The reflectance contrast (relative to water) of the delineated oil slick at ~1600 nm (1609 nm for OLI and 1614 nm for MSI) was inspected, yet no oil emulsions were found in any cloud-free images used in this study (Table 1). This does not suggest that oil emulsions did not occur; an oil emulsion patch could be too small to be captured by the relatively large pixels ($30 \times 30 \text{ m}^2$ for OLI and $20 \times 20 \text{ m}^2$ for MSI SWIR bands). On the other hand, even if the size of the thick emulsion is much smaller than a pixel size, (i.e., $30 \times 30 \text{ m}^2$ for OLI), the oil slick (including both thin oil and thick emulsion) can still be larger than a pixel. A rule of thumb has been used in the past, in which thick oil occupies only 10% of the oil slick area, while 90% of the area is composed of thin oil sheens (NOAA, 2016). A recent study from the DWH oil spill (Sun et al., 2016) showed that thick oil ($> 200 \mu\text{m}$) occupied only 5% of the total area covered by thicker than sheen oil slicks. Statistical analysis of the delineated slicks from the present study shows that 92% of the slicks have an area $> 1 \text{ km}^2$ (Fig. 5c), which corresponds to > 1100 Landsat pixels ($30 \times 30 \text{ m}^2$). Moreover, same-day image pair of OLI (30 m resolution) and MSI (10 m resolution) images (time difference of 15 min, Fig. 8a and b) do not show large differences in the delineated oil slick area. Based on the analysis above, we are confident that the 30-m spatial resolution used here is sufficient for oil slick detection in the MC-20 region.

The question then becomes whether the oil discharge volume can be estimated from these observations. Here we attempted this challenge using field measurements and empirical values published in the literature. Specifically: 1) Various oil thicknesses have been reported from cruise surveys, ranging from rainbow sheens, to dark fresh oil, and thick emulsions (Herbst et al., 2016; Garcia-Pineda, 2016). Several oil thickness-color codes have been developed to visually estimate oil thicknesses based on oil's color appearance, including the Bonn Agreement Oil Appearance Code (2017) and American Society of Test Materials (ASTM F2534-17, 2017) code. The ASTM code is widely used as a guide in oil spill responses, providing information criteria for estimating oil thicknesses using visual clues, but the ASTM guide is only applicable to thin sheens up to about 3 μm (see ASTM F2534-17, 2017). In this study, we used the oil thickness table from the Bonn Agreement (2017) and NOAA (2016), which distinguishes thick and thin oil in appearance and gives thickness ranges for both thick and thin oil. The Bonn Agreement code has been widely used in recent studies (Leifer et al., 2012; Jones and Holt, 2018; Svejksky et al., 2016) and in industrial oil spill responses (IPIECA-IOPG, 2015). NOAA (2016) has adapted the Bonn Agreement (2017) code with slight differences in oil "Sheens" category, now corresponding to oil thicknesses up to 5 μm . In

Table 5
Input parameters to Eq. (2) and the calculated daily oil discharge rate.

| | Area (km ² / day) | Sheens- thickness (μm) | Metallic- thickness (μm) | Residence- time (hours) | V _d (m ³ / day) | V _d (US barrels/ day) |
|-------------|------------------------------------|------------------------------|--------------------------------|-------------------------------|---|--|
| Lower Bound | 7.1 | 0.04 | 5 | 6.4 | 7.7 | 48 |
| Upper Bound | 22.7 | 5 | 50 | 14.4 | 274.1 | 1724 |

In this study, we adopt the thickness ranges from NOAA (2016) category of “Sheens” for thin oil and “Metallic” for thick oil. “Sheens” is in the range of 0.04–5 μm with grey/silver to rainbow-appearance while thicker than sheens “Metallic” oil (reflect the color of the sky but with some element of oil color) is in the range of 5–50 μm (NOAA, 2016). 2) A ratio of thick to thin oil of 5:95 from a previous study on the DWH oil spill (Sun et al., 2016) was adopted for thickness estimation in this study; 3) From a hindcast model based on various wind and current conditions over the natural hydrocarbon seeps around the Green Canyon 600 lease block in the northern GoM, average slick surface residence-time was estimated to be 6.4 h while slicks of > 10 km in length had an average surface residence-time of 14.4 h (Daneshgar Asl et al., 2017). The two residence times here were assumed to be applicable to oil slicks around the MC-20 site on the lower and upper bounds of the average oil footprint size per day: 14.9 * (1 ± 0.523) km², where the relative uncertainty term in the parenthesis came from the same-day cross-check between image pairs. Then, assuming dynamic balance and continuous oil release, the daily oil discharge rate (V_d) was estimated as:

$$V_d = \text{Area} \times (5\% \times \text{Metallic} - \text{Thickness} + 95\% \times \text{Sheen} - \text{Thickness}) \times 24 \text{ h} / (\text{Residence} - \text{Time} - \text{in} - \text{hours}) \quad (2)$$

The inputs to Eq. (2) are listed in Table 5. After converting to US barrels, the calculated average V_d is in the range of 48–1724 barrels/day. Given the factors impacting the oil detection accuracy (due to lack of strong sun glint half of the year), this range is likely to be biased low. The same can be said for the cumulative oil footprint and average oil slick size. Therefore, the average daily oil discharge ranging from 48 to ~1700 US barrels per day represents a conservative estimate if all assumptions used in the calculation are reasonable.

5. Conclusions

Using optical remote sensing imagery from Landsat TM, ETM+, OLI and Sentinel-2A MSI, oil slicks around the MC-20 well site in the northern Gulf of Mexico were objectively assessed for the first time after the hurricane-induced damage of the oil platform and wells in September 2004. The results show that the percentage of cloud-free images containing oil slicks around the MC-20 site has increased from ~40% in 2005, ~70% in 2006–2011, to > 80% since 2012, suggesting an increase in oil discharge in recent years. From 2005 to 2016, about 14.9 km² of the area surrounding the MC-20 site is covered by oil on an average day, with a cumulative oil footprint of ~1900 km² and an estimated daily discharge volume ranging from 48 to ~1700 barrels.

Having observations in the same day (or a few consecutive days from different sensors) improves the understanding of oil slick movement over short temporal periods, especially in this region influenced by a large river plume. For the most part, oil slick distribution agrees well with circulation patterns that are largely controlled by the Mississippi River plume, but can also be affected by direct wind forcing. The locations of the river induced fronts with respect to the oil source also contribute to both onshore propagation and longer-term pathways of the hydrocarbons. Moreover, wind forces may dominate the oil spreading process when the Mississippi River plume does not encompass the MC-20 site.

Acknowledgments

This study was made possible in part by the BP/Gulf of Mexico Research Initiative (awards GOMA 23160700 and C-IMAGE II) and in part by a NASA Earth and Space Science Fellowship (NESSF, grant NNX16AN95H). Data are publicly available through the Gulf of Mexico Research Initiative Information & Data Cooperative (GRIIDC) at <https://data.gulfresearchinitiative.org> (doi: <https://doi.org/10.7266/N7M9072W>). We thank the USGS for providing Landsat data, which are openly accessible from <https://earthexplorer.usgs.gov/>, NOAA for providing NCEP wind data, which are openly accessible from <https://www.esrl.noaa.gov/psd/data/gridded/data.ncep.reanalysis2.html>, ESA for providing Sentinel-2 MSI data, which are openly accessible from <https://scihub.copernicus.eu>, and NASA for providing MODIS and chlorophyll-a concentration data, which are openly accessible from <https://oceancolor.gsfc.nasa.gov/>. M. Le Hénaff acknowledges partial support from the Physical Oceanography Division at NOAA's Atlantic Oceanographic and Meteorological Laboratory, AOML. We thank Dr. HeeSook Kang for preparing the current model fields, and we acknowledge the help from Brock Murch (University of South Florida) to improve the presentation of the manuscript. Three anonymous reviewers also provided comments to help improve the manuscript.

References

- Adamo, M., De Carolis, G., De Pasquale, V., Pasquariello, G., 2009. Detection and tracking of oil slicks on sun-glittered visible and near infrared satellite imagery. *Int. J. Remote Sens.* 30 (24), 6403–6427. <https://doi.org/10.1080/01431160902865772>.
- Androulidakis, Y.S., Kourafalou, V.H., 2013. On the processes that influence the transport and fate of Mississippi waters under flooding outflow conditions. *Ocean Dyn.* 63 (2–3), 143–164.
- Androulidakis, Y.S., Kourafalou, V.H., Schiller, R.V., 2015. Process studies on the evolution of the Mississippi River plume: impact of topography, wind and discharge conditions. *Cont. Shelf Res.* 107, 33–49.
- Androulidakis, Y., Kourafalou, V.H., Özgökmen, T., Garcia-Pineda, O., Lund, B., Le Hénaff, M., Hu, C., Haus, B.K., Novelli, G., Guigand, C., Kang, H., Hole, L., Horstmann, J., 2018. Influence of river induced fronts on hydrocarbon transport: a multi-platform observational study. *J. Geophys. Res. Oceans* 123, 3259–3285.
- ASTM F2534-17, 2017. Standard Guide for Visually Estimating Oil Spill Thickness on Water. ASTM International, West Conshohocken, PA. www.astm.org.
- Bleck, R., 2002. An oceanic general circulation model framed in hybrid isopycnal-Cartesian coordinates. *Ocean Model* 4, 55–88.
- Bonn Agreement, 2017. Bonn agreement aerial operations handbook. Publication of the Bonn Agreement, April 2016. Retrieved on July 24, 2018 from. https://www.bonnagreement.org/site/assets/files/17600/ao_h_part_iii_guidelines_detection_investigation_evaluation.pdf.
- Brekke, C., Solberg, A.H.S., 2005. Oil spill detection by satellite remote sensing. *Remote Sens. Environ.* 95 (1), 1–13. <https://doi.org/10.1016/j.rse.2004.11.015>.
- Bulgarelli, B., Djavidnia, S., 2012. On MODIS retrieval of oil spill spectral properties in the marine environment. *IEEE Geosci. Remote Sens. Lett.* 9 (3), 398–402. <https://doi.org/10.1109/LGRS.2011.2169647>.
- Bureau of Safety and Environmental Enforcement, 2017. Taylor Energy oil discharge at MC-20 site and ongoing response efforts. Retrieved June 30, 2017 from. <https://www.bsee.gov/newsroom/library/incident-archive/taylor-energy-mississippi-canyon/ongoing-response-efforts>.
- Byfield, V., 1998. Optical Remote Sensing of Oil in the Marine Environment (Doctoral dissertation). University of Southampton.
- Chassignet, E.P., Hurlburt, H.E., Smedstad, O.M., Halliwell, G.R., Wallcraft, A.J., Metzger, E.J., Blanton, B.O., Lozano, C., Rao, D.B., Hogan, P.J., Srinivasan, A., 2006. Generalized vertical coordinates for eddy-resolving global and coastal ocean forecasts. *Oceanography* 19 (1), 118–129. <https://doi.org/10.5670/oceanog.2006.95>.
- Clark, R.N., Swayze, G.A., Leifer, I., Livo, K.E., Kokaly, R., Hoefen, T., Lundeen, S., Eastwood, M., Green, R.O., Pearson, N., 2010. A method for quantitative mapping of thick oil spills using imaging spectroscopy. In: US Geological Survey Open-File Report. vol. 1167. pp. 1–51.
- Cox, C., Munk, W., 1954. Measurement of the roughness of the sea surface from photographs of the sun's glitter. *J. Opt. Soc. Am.* 44 (11), 838–850. <https://doi.org/10.1364/JOSA.44.000838>.
- Daneshgar Asl, S., Amos, J., Woods, P., Garcia-Pineda, O., MacDonald, I.R., 2016. Chronic, anthropogenic hydrocarbon discharges in the Gulf of Mexico. *Deep-Sea Res. II Top. Stud. Oceanogr.* 129, 187–195.
- Daneshgar Asl, S., Dukhovskoy, D.S., Bourassa, M., MacDonald, I.R., 2017. Hindcast modeling of oil slick persistence from natural seeps. *Remote Sens. Environ.* 189, 96–107. <https://doi.org/10.1016/j.rse.2016.11.003>.
- Feng, L., Hu, C., 2016. Comparison of valid ocean observations between MODIS Terra and Aqua over the global oceans. *IEEE Trans. Geosci. Remote Sens.* 54, 1575–1585.
- Garcia-Pineda, O., 2016. Taylor. Retrieved March 6, 2018 from. <https://www.youtube.com/watch?v=RlaXOTg3IU>.

- Garcia-Pineda, O., MacDonald, I., Zimmer, B., 2008. Synthetic aperture radar image processing using the supervised textural-neural network classification algorithm. In: Paper presented at IGARSS 2008, IEEE International Geoscience and Remote Sensing Symposium, 7–11 July 2008.
- Garcia-Pineda, O., Zimmer, B., Howard, M., Pichel, W., Li, X., MacDonald, I.R., 2009. Using SAR images to delineate ocean oil slicks with a texture-classifying neural network algorithm (TCNNA). *Can. J. Remote. Sens.* 35 (5), 411–421. <https://doi.org/10.5589/m09-035>.
- Garcia-Pineda, O., MacDonald, I., Zimmer, B., Shedd, B., Roberts, H., 2010. Remote-sensing evaluation of geophysical anomaly sites in the outer continental slope, northern Gulf of Mexico. *Deep-Sea Res. II Top. Stud. Oceanogr.* 57 (21–23), 1859–1869. <https://doi.org/10.1016/j.jdsr.2010.05.005>.
- Garvine, R.W., Monk, J.D., 1974. Frontal structure of a river plume. *J. Geophys. Res.* 79 (15), 2251–2259.
- Halliwell, G.R., Barth, A., Weisberg, R.H., Hogan, P.J., Smedstad, O.M., Cummings, J., 2009. Impact of GODAE products on nested HYCOM simulations of the West Florida Shelf. *Ocean Dyn.* 59, 139–155. <https://doi.org/10.1007/s10236-008-0173-2>.
- Herbst, L., DeCola, E., Kennedy, K., 2016. New pathways for developing and testing oil spill response equipment in real world conditions. In: Paper Presented at OCEANS 2016 MTS/IEEE, Monterey, CA, 19–23 Sept. 2016.
- Hu, C., Li, X., Pichel, W.G., Muller-Karger, F.E., 2009. Detection of natural oil slicks in the NW Gulf of Mexico using MODIS imagery. *Geophys. Res. Lett.* 36 (1). <https://doi.org/10.1029/2008gl036119>.
- Hu, C., Weisberg, R.H., Liu, Y., Zheng, L., Daly, K., English, D., Zhao, J., Vargo, G., 2011. Did the northeastern Gulf of Mexico become greener after the Deepwater Horizon oil spill? *Geophys. Res. Lett.* 38, L09601. <https://doi.org/10.1029/2011GL047184>.
- Hu, C., Feng, L., Hardy, R.F., Hochberg, E.J., 2015. Spectral and spatial requirements of remote measurements of pelagic *Sargassum* macroalgae. *Remote Sens. Environ.* 167, 229–246. <https://doi.org/10.1016/j.rse.2015.05.022>.
- IPIECA-IOGP, 2015. Aerial observation of oil spills at sea. London, February 2015: IPIECA-IOGP. Retrieved from: <http://www.ipieca.org/resources/good-practice/aerial-observation-of-oil-spills-at-sea/>.
- Jackson, C.R., Alpers, W., 2010. The role of the critical angle in brightness reversals on sunglint images of the sea surface. *J. Geophys. Res.* 115 (C9). <https://doi.org/10.1029/2009jc006037>.
- Jones, C.E., Holt, B., 2018. Experimental L-band airborne SAR for oil spill response at sea and in coastal waters. *Sensors* 18 (2), 641. <https://doi.org/10.3390/s18020641>.
- Kourafalou, V.H., Androulidakis, Y.S., 2013. Influence of Mississippi River induced circulation on the Deepwater Horizon oil spill transport. *J. Geophys. Res. Oceans* 118 (8), 3823–3842.
- Kourafalou, V.H., Oey, L.-Y., Wang, J.D., Lee, T.N., 1996. The fate of river discharge on the continental shelf. Part I: modeling the river plume and the inner-shelf coastal current. *J. Geophys. Res. Oceans* 101 (C2), 3415–3434. <https://doi.org/10.1029/95JC03024>.
- Kourafalou, V.H., Peng, G., Kang, H., Hogan, P.J., Smedstad, O.M., Weisberg, R.H., 2009. Evaluation of global ocean data assimilation experiment products on South Florida nested simulations with the hybrid coordinate ocean model. *Ocean Dyn.* 59 (1), 47–66. <https://doi.org/10.1007/s10236-008-0160-7>.
- Le Hénaff, M., Kourafalou, V.H., 2016. Mississippi waters reaching South Florida reefs under no flood conditions: synthesis of observing and modeling system findings. *Ocean Dyn.* 66 (3), 435–459.
- Le Hénaff, M., Kourafalou, V.H., Paris, C.B., Helgers, J., Hogan, P.J., Srinivasan, A., 2012. Surface evolution of the Deepwater Horizon oil spill: combined effects of circulation and wind induced drift. *Environ. Sci. Technol.* 46, 7267–7273. <https://doi.org/10.1021/es301570w>.
- Leifer, I., Lehr, W.J., Simecek-Beatty, D., Bradley, E., Clark, R., Dennison, P., Hu, Y., Matheson, S., Jones, C.E., Holt, B., Reif, M., Roberts, D.A., Svejksky, J., Swayze, G., Wozencraft, J., 2012. State of the art satellite and airborne marine oil spill remote sensing: application to the BP Deepwater Horizon oil spill. *Remote Sens. Environ.* 124 (0), 185–209. <https://doi.org/10.1016/j.rse.2012.03.024>.
- Liu, Y., Weisberg, R.H., Hu, C., Kovach, C.C., Riethmüller, R.R., 2013. Evolution of the Loop Current system during the Deepwater Horizon oil spill event as observed with drifters and satellites. In: Liu, Y., Macfadyen, A., Ji, Z., Weisberg, R.H. (Eds.), *Monitoring and modeling the Deepwater Horizon oil spill: a record-breaking enterprise*, pp. 91–101.
- Lu, Y., Li, X., Tian, Q., Zheng, G., Sun, S., Liu, Y., Yang, Q., 2013a. Progress in marine oil spill optical remote sensing: detected targets, spectral response characteristics, and theories. *Mar. Geod.* 36 (3), 334–346. <https://doi.org/10.1080/01490419.2013.793633>.
- Lu, Y., Tian, Q., Wang, X., Zheng, G., Li, X., 2013b. Determining oil slick thickness using hyperspectral remote sensing in the Bohai Sea of China. *Int. J. Digital Earth* 6, 76–93.
- Lu, Y., Sun, S., Zhang, M., Murch, B., Hu, C., 2016. Refinement of the critical angle calculation for the contrast reversal of oil slicks under sunglint. *J. Geophys. Res. Oceans* 121 (1), 148–161. <https://doi.org/10.1002/2015jc011001>.
- Macdonald, I.R., Guinasso, N.L., Ackleson, S.G., Amos, J.F., Duckworth, R., Sassen, R., Brooks, J.M., 1993. Natural oil slicks in the Gulf of Mexico visible from space. *J. Geophys. Res.* 98 (C9), 16351. <https://doi.org/10.1029/93jc01289>.
- MacDonald, I.R., et al., 2015. Natural and unnatural oil slicks in the Gulf of Mexico. *J. Geophys. Res. Oceans* 120 (12), 8364–8380. <https://doi.org/10.1002/2015JC011062>.
- McNutt, M.K., Camilli, R., Crone, T.J., Guthrie, G.D., Hsieh, P.A., Ryerson, T.B., Savas, O., Shaffer, F., 2012. Review of flow rate estimates of the Deepwater Horizon oil spill. *Proc. Natl. Acad. Sci.* 109 (50), 20260–20267. <https://doi.org/10.1073/pnas.1112139108>.
- Murphy, D., Gemmill, B., Vaccari, L., Li, C., Bacosa, H., Evans, M., Gemmill, C., Harvey, T., Jalali, M., Niepa, T.H., 2016. An in-depth survey of the oil spill literature since 1968: long term trends and changes since Deepwater Horizon. *Mar. Pollut. Bull.* 113, 371–379.
- National Response Center, 2018. Oil spill, chemical release or maritime security incident report. Retrieved July 17, 2018 from: <http://www.nrc.uscg.mil>.
- NOAA, 2013. Taylor Energy platform “Saratoga”. In: National Oceanic and Atmospheric Administration Incident News, Retrieved on 9 August 2018 from: <https://incidentnews.noaa.gov/incident/8634>.
- NOAA, 2016. Open Water Oil Identification Job Aid for Aerial Observation. With Standardized Oil Slick Appearance and Structure Nomenclature and Codes. NOAA Office of Response and Restoration, Emergency Response Division, Seattle, Washington, pp. 1–51. Retrieved from: https://response.restoration.noaa.gov/sites/default/files/OWJA_2016.pdf.
- Schiller, R.V., Kourafalou, V.H., 2010. Modeling river plume dynamics with the HYbrid Coordinate Ocean Model. *Ocean Model* 33 (1–2), 101–117.
- Schiller, R.V., Kourafalou, V.H., Hogan, P., Walker, N.D., 2011. The dynamics of the Mississippi River plume: impact of topography, wind and offshore forcing on the fate of plume waters. *J. Geophys. Res. Oceans* 116 (C6). <https://doi.org/10.1029/2010JC006883>.
- Sun, S., Hu, C., 2016. Sun glint requirement for the remote detection of surface oil films. *Geophys. Res. Lett.* 43, 309–316.
- Sun, S., Hu, C., Tunnell, J.W., 2015. Surface oil footprint and trajectory of the Ixtoc-1 oil spill determined from Landsat/MSS and CZCS observations. *Mar. Pollut. Bull.* 101 (2), 632–641. <https://doi.org/10.1016/j.marpolbul.2015.10.036>.
- Sun, S., Hu, C., Feng, L., Swayze, A.S., Holmes, J., Graettinger, G., MacDonald, I., Garcia, O., Leifer, I., 2016. Oil slick morphology derived from AVIRIS measurements of the Deepwater horizon oil spill: implications for spatial resolution requirements of remote sensors. *Mar. Pollut. Bull.* 103 (1–2), 276–285. <https://doi.org/10.1016/j.marpolbul.2015.12.003>.
- Sun, S., Lu, Y., Liu, Y., Wang, M., Hu, C., 2018. Tracking an oil tanker collision and spilled oils in the East China Sea using multisensor day and night satellite imagery. *Geophys. Res. Lett.* 45, 3212–3220.
- Svejksky, J., Lehr, W., Muskat, J., Graettinger, G., Mullin, J., 2012. Operational utilization of aerial multispectral remote sensing during oil spill response. *Photogramm. Eng. Remote. Sens.* 78 (10), 1089–1102.
- Svejksky, J., Hess, M., Muskat, J., Nedwed, T.J., McCall, J., Garcia, O., 2016. Characterization of surface oil thickness distribution patterns observed during the Deepwater Horizon (MC-252) oil spill with aerial and satellite remote sensing. *Mar. Pollut. Bull.* 110 (1), 162–176. <https://doi.org/10.1016/j.marpolbul.2016.06.066>.
- United States of America v. BP Exploration and Production, Inc, et al., 2015. Findings of fact and conclusions of law: phase two trial. In re: oil spill by the oil rig “Deepwater Horizon”. In: *The Gulf of Mexico, on April 20, 2010, No. MDL 2179, 2015 WL 225421 (L.A.E.D. Jan. 15, 2015). (Doc. 14021). U.S. District Court for the Eastern District of Louisiana Retrieved from: http://www.laed.uscourts.gov/OilSpill/Orders/1152015FindingsPhaseTwo.pdf*.
- Walker, N.D., Wiseman Jr., W.J., Rouse Jr., L.J., Babin, A., 2005. Effects of river discharge, wind stress, and slope eddies on circulation and the satellite-observed structure of the Mississippi River plume. *J. Coast. Res.* 21 (6), 1228–1244.
- Walker, N.D., Pilley, C.T., Raghunathan, V.V., D’Sa, E.J., Leben, R.R., Hoffman, N.G., Brickley, P.J., Coholan, P.D., Sharma, N.N., Graber, H.C., Turner, R.E., 2011. Impacts of Loop Current frontal cyclonic eddies and wind forcing on the 2010 Gulf of Mexico oil spill. In: *Monitoring and Modeling the Deepwater Horizon Oil Spill: A Record-breaking Enterprise*. American Geophysical Union, Washington, D. C. <https://doi.org/10.1029/2011GM001120>.
- Warren, C.J., MacFadyen, A., Henry, C., 2014. Mapping oil for the destroyed Taylor Energy site in the Gulf of Mexico. In: *International Oil Spill Conference Proceedings*. vol. 2014, No. 1. pp. 299931.
- Wettle, M., Daniel, P.J., Logan, G.A., Thankappan, M., 2009. Assessing the effect of hydrocarbon oil type and thickness on a remote sensing signal: a sensitivity study based on the optical properties of two different oil types and the HYMAP and Quickbird sensors. *Remote Sens. Environ.* 113 (9), 2000–2010. <https://doi.org/10.1016/j.rse.2009.05.010>.
- Zhang, X., Hetland, R.D., Marta-Almeida, M., DiMarco, S.F., 2012. A numerical investigation of the Mississippi and Atchafalaya freshwater transport, filling and flushing times on the Texas-Louisiana Shelf. *J. Geophys. Res. Oceans* 117, C11009. <https://doi.org/10.1029/2012JC008108>.